

IMMUNOTHERAPY

In-depth tissue profiling using multiplexed immunohistochemical consecutive staining on single slide

Romain Remark,¹ Taha Merghoub,² Niels Grabe,³ Geert Litjens,³ Diane Damotte,^{4,5} Jedd D. Wolchok,² Miriam Merad,^{1*} Sacha Gnajic^{1*}

2016 © The Authors,
some rights reserved;
exclusive licensee
American Association
for the Advancement
of Science.
10.1126/scimmunol.aaf6925

Despite remarkable recent achievements of immunotherapy strategies in cancer treatment, clinical responses remain limited to subsets of patients. Predictive markers of disease course and response to immunotherapy are urgently needed. Recent results have revealed the potential predictive value of immune cell phenotype and spatial distribution at the tumor site, prompting the need for multidimensional immunohistochemical analyses of tumor tissues. To address this need, we developed a sample-sparing, highly multiplexed immunohistochemistry technique based on iterative cycles of tagging, image scanning, and destaining of chromogenic substrate on a single slide. This assay, in combination with a newly developed automated digital landscaping solution, democratizes access to high-dimensional immunohistochemical analyses by capturing the complexity of the immune system using routine pathology standards. Applications of the method extend beyond cancer to screen and validate comprehensive panels of tissue-based prognostic and predictive markers, perform in-depth *in situ* monitoring of therapies, and identify targets of disease.

INTRODUCTION

The immune system is formed by an incredibly diverse network of cells derived from the myeloid and lymphoid hematopoietic lineages that cooperate to sense and respond to tissue injury signals. Recent studies have revealed that immune cell types initially believed to represent a single lineage actually consist of different subpopulations with distinct functions (1), and the nature of the responding immune cells and their spatial organization within organs control the development of effective immune responses (2, 3). However, a lack of solutions to characterize this complexity at the tissue site hampers our ability to perform comprehensive analyses of ongoing immune responses and to decipher *in situ* mechanisms at play.

In cancer, evidence of immunocompetence at the tumor site has been associated with improved outcome of patients with various tumor types (4, 5), and several studies established that high lymphocyte infiltration in tumors is prognostic of progression-free or overall survival (6, 7). A landmark study in colon cancer lesions demonstrated that the density of two lymphocyte populations (CD3/CD8, CD3/CD45RO, or CD8/CD45RO) in two tumor regions (center and invasive margin) is a better predictor of survival than the tumor-node-metastasis (TNM) stage (6, 8). As a result, pathologists around the world are developing a task force to validate the use of CD3/CD8 infiltration, named “Immunoscore,” to complement standard staging in routine clinical cancer settings (9). The sole measurement of CD3/CD8 cell infiltration in tumors, although useful in colorectal cancer, is not predictive in all solid tumors, where other immune cell populations might be associated

with favorable clinical outcome (10–12), revealing the critical need for a more comprehensive analysis of the immune microenvironment of tumor tissues.

In addition to the powerful prognostic value of tumor-associated immune cells, recent studies have established that antibody (Ab)-mediated blockade of immune checkpoint receptors on T cells, or their ligands on antigen-presenting cells such as dendritic cells (DCs) or macrophages, can lead to significant clinical responses in a subset of patients (13). Three checkpoint inhibitors have been actively explored clinically, including Abs to the checkpoint receptor cytotoxic lymphocyte antigen 4 (CTLA-4), programmed cell death 1 (PD-1), and the checkpoint ligand programmed death ligand 1 (PD-L1) (14). Analysis of tumor lesions treated with checkpoint blockade revealed that a preexisting high density of CD8⁺ T cells in the center and invasive margin of the tumor mass, along with expression of PD-L1 on infiltrating immune cells or tumor cells, correlates with increased tumor response to anti-PD-1 and anti-PD-L1 Abs (15, 16). These results beg for the inclusion of longitudinal high-dimensional analysis of tumor lesions in the immune monitoring of cancer patients (17).

The visualization and quantification of different immune cellular subsets require the use of complex phenotypic marker combinations. A major limitation for such high-dimensional analyses is tumor tissue availability. Most clinical pathology laboratories use chromogenic immunohistochemistry (IHC) on commonly accessible formalin-fixed, paraffin-embedded (FFPE) tissues and stain for no more than two markers per tissue slide (9). Several commercial multiplexed immunostaining methods have been developed to allow high-dimensional analysis of complex immune cell populations, but most of these methods have inherent limitations, including the use of proprietary fluorescent probes that stray from accepted standards in pathology; the dependency on frozen material; the associated tissue destruction; and the requirement of costly equipment, materials, and reagents (18–22).

To address the clinical need for high-dimensional analysis of tissue lesions in clinical pathology, we sought to develop a multiplexed chromogen-based IHC staining assay independent of proprietary equipment that could be readily integrated in routine clinical pathology. This

¹Division of Hematology and Oncology, Tisch Cancer Institute, Icahn School of Medicine at Mount Sinai, New York, NY 10029, USA. ²Sloan Kettering Institute, Memorial Sloan Kettering Cancer Center, New York, NY 10065, USA. ³Department of Medical Oncology at National Center for Tumor Diseases, University Hospital Heidelberg and Hamamatsu Tissue Imaging and Analysis Center, BIOPQUANT, University of Heidelberg, Heidelberg, Germany. ⁴INSERM U1138, Team “Cancer, Immune Control and Escape” Cordeliers Research Center, Paris, France. ⁵Department of Pathology, Cochin Hospital, AP-HP, Paris, France.

*These authors contributed equally to this work.

†Corresponding author. Email: miriam.merad@mssm.edu (M.M.); sacha.gnjatic@mssm.edu (S.G.)

new technique, named multiplexed immunohistochemical consecutive staining on single slide (MICSSS), can be performed on any FFPE tissue using iterative cycles of staining, image scanning, and destaining of chromogenic substrate and enables characterization of large panels of parameters on one single tissue section, including colocalization of markers on single cells while preserving tissue antigenicity and architecture. Last, an automated digital landscaping software based on deep learning was designed, developed, and applied to this multiplexed IHC method, thus facilitating the ability to automatically map and analyze the complexity of the tumor microenvironment (TME). Here, we describe the MICSSS workflow and its clinical potential to identify prognostic and predictive factors of disease course or predictive biomarkers of response to immunotherapy.

RESULTS

A multiplexed IHC method was developed for iterative chromogen staining on a single paraffin-embedded tissue slide

Because a very limited number of chromogens can be used in parallel on one same tissue slide, due to the paucity of available enzymatic substrates, we asked whether consecutive cycles of Ab staining, image scanning, destaining of chromogen, blocking, and restaining could help better characterize the complexity of the TME (Fig. 1A).

Thus, one single slide of FFPE tumor tissue section was first stained with a standard primary Ab followed by a biotin-linked secondary Ab and horseradish peroxidase (HRP)-conjugated streptavidin to amplify the signal. Peroxidase-labeled compounds were revealed using 3-amino-9-ethylcarbazole (AEC), an aqueous substrate that results in red staining, and counterstained using hematoxylin (blue). The slide was mounted for microscopy and scanned at high resolution by digital imaging. The colored reaction product was then

removed using an organic solvent-based destaining buffer after coverslip removal. Figure 1B shows a CD20 B cell follicle staining followed by a chemical destaining. Because the Abs were not stripped completely by the destaining or the antigen retrieval steps, as shown by the ability to restain slides directly with AEC substrate (fig. S1), the destained slide was treated with a blocking buffer (fig. S1) before the next cycle of staining to prevent any remnant reactivity to primary or secondary Abs used in the first cycle. This allowed performing up to 10 cycles of staining/image scanning/destaining on the same FFPE tissue slide (Fig. 1B). The destaining/staining/scanning process took 6 to 7 hours per cycle, and at least 30 samples were concomitantly processed manually, whereas a much higher number of slides could be processed with staining automation.

MICSSS helps characterize the spatial distribution of complex cell populations in tumor tissues without cross-reactivity between iterative staining cycles

To examine whether the MICSSS assay can be used to comprehensively assess the diversity of the immune microenvironment of tumor tissues, we stained FFPE colorectal tumor tissue lesions with hematoxylin together with markers of diverse immune cell lineages, including markers of lymphoid and myeloid cells. We used the T cell markers CD2, CD3, and CD8, the B cell marker CD20, the transcription factor enriched in T regulatory cells FoxP3 (forkhead box P3), the myeloid cell marker DC lysosome-associated membrane protein (DC-LAMP), and the nuclear proliferation marker Ki-67, to assess the functional state of T and B cell populations. Abs were applied consecutively, and the slides were scanned after each staining following the method described in Fig. 1A. For each marker, a virtual layer was selected on the basis of the chromogen color from individual captured images. Each layer was assigned an artificial color to help distinguish different

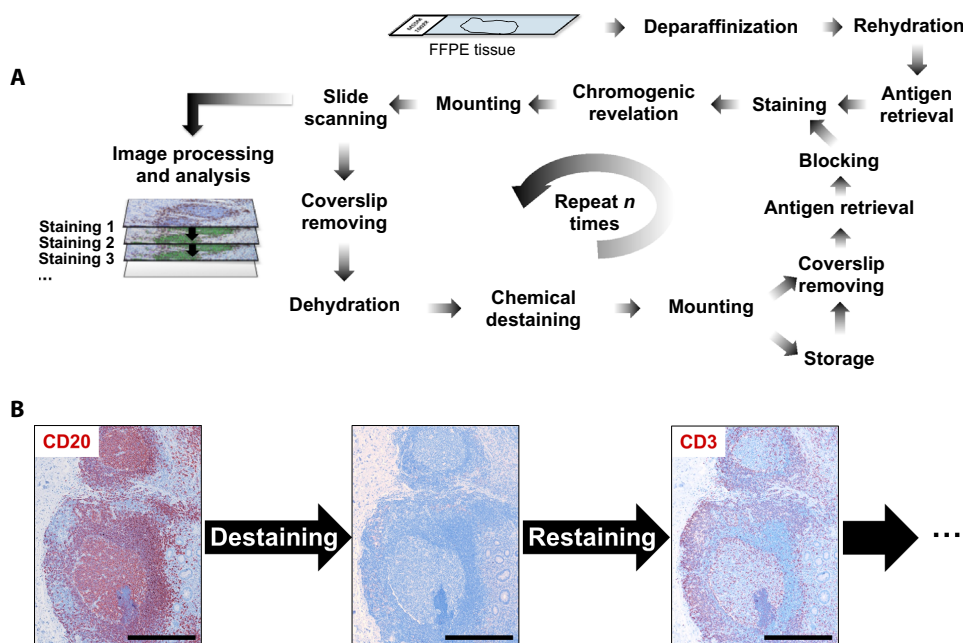


Fig. 1. MICSSS workflow. (A) MICSSS protocol. FFPE tissue sections ($5\ \mu\text{m}$) were incubated with primary Abs followed by biotinylated secondary Abs, streptavidin-HRP, and AEC. Stained tissue sections were counterstained, mounted, and scanned. After each scanning procedure, the slide coverslip was removed, and AEC chromogen was dissolved. Tissue sections underwent antigen retrieval and were then incubated in a blocking buffer before the initiation of a new staining cycle. (B) A $5\ \mu\text{m}$ FFPE gut section obtained from an ulcerative colitis patient was stained with anti-CD20 Ab and destained and stained with anti-CD3 Ab following the MICSSS workflow. The exact same tissue can be stained several times using the MICSSS method. Scale bars, $0.5\ \text{mm}$.

markers when overlaid in a composite figure. To improve the visualization of colocalized markers, bright-field images were inverted in image processing software and red green blue (RGB) channels were separated to generate fluorescent-like images. As shown in Fig. 2, the expression of nuclear, cytoplasmic, and membranous markers can be assessed independently or simultaneously to identify complex cell populations such as CD3⁺ CD8⁻ FoxP3⁺ Ki-67⁺ T cells. Using the Manders' overlap coefficient (tM) with threshold set by Costes method as a measure of colocalization, we observed a high degree of colocalization between markers known to be expressed by the same cellular compartment [for example, tM_(CD8/CD3) = 0.864, tM_(CD3/CD2) = 0.887, and tM_(CD8/CD2) = 0.842], and a low degree of

colocalization between markers expressed by different immune cell populations [for example, tM_(CD20/CD3) = 0.063, tM_(CD20/CD8) = 0.066, and tM_(CD20/DC-LAMP) = 0.023].

No cross-reactivity was observed between secondary Abs targeting primary Abs from the same species or with the same isotype. The absence of cross-reactivity was dependent on incubation with a blocking buffer before each restaining step (fig. S1).

MICSSS does not decrease antigenicity or generate steric hindrance

One potential caveat of repetitive destaining/restaining method is the potential alteration of tissue integrity and antigen expression. To

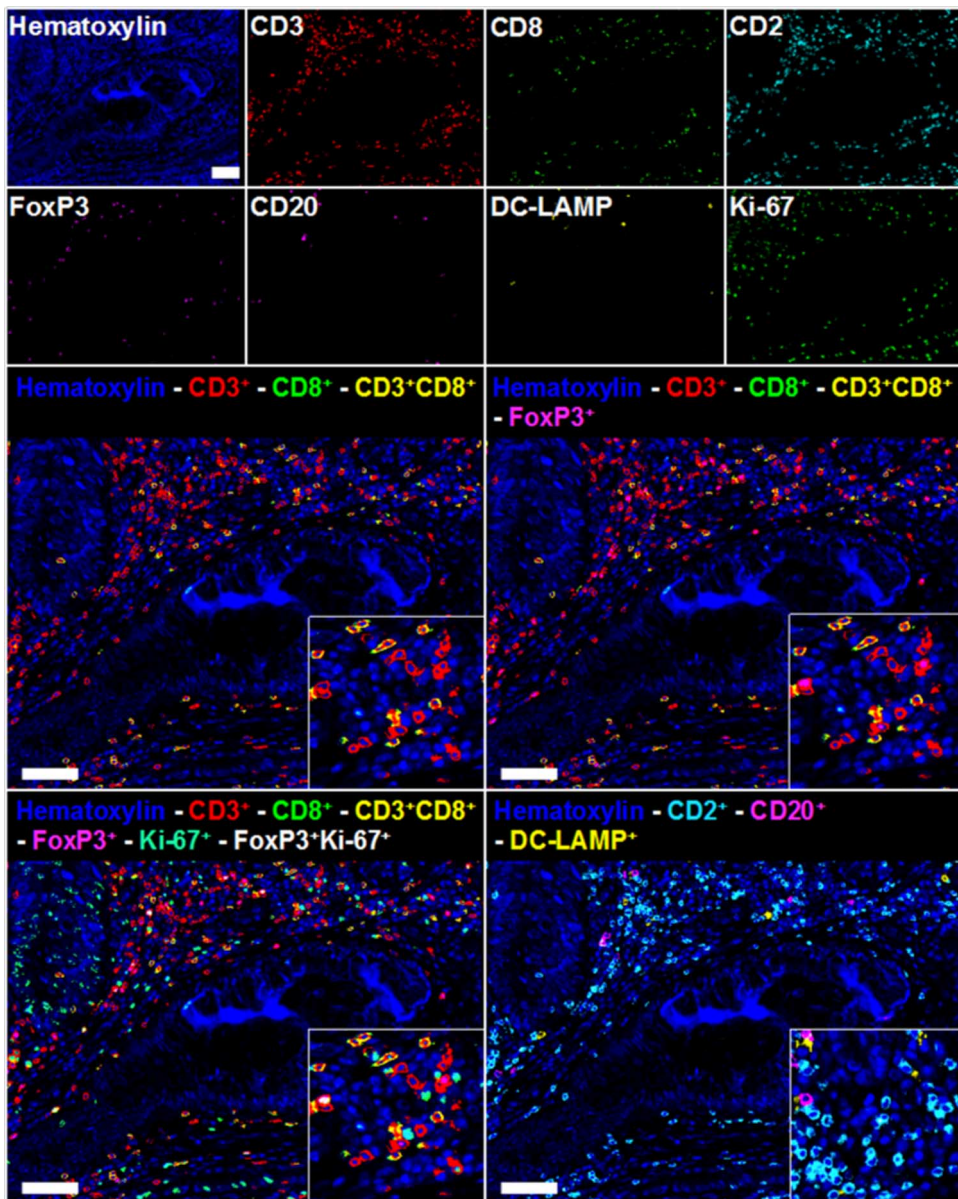


Fig. 2. MICSSS helps characterize the tumor immune microenvironment. Colorectal cancer tissue section was sequentially stained and scanned for hematoxylin, CD3, CD8, CD2, FoxP3, CD20, DC-LAMP, and Ki-67. Bright-field images were inverted, and RGB channel splitting was performed. Upper panels show single staining for each individual staining. Some selected images were merged, and pseudocolors were attributed to each marker (lower panels). Immune cells were mostly localized in the stroma surrounding the tumor islets. Right insets show magnifications of single-positive, double-positive (for example, CD3⁺ CD8⁺ or CD3⁺ FoxP3⁺), or triple-positive (for example, CD3⁺ FoxP3⁺ Ki-67⁺) cells, allowing an accurate determination of cell phenotype and state. Scale bars, 50 μ m.

address this question, we stained and destained normal lung epithelium and did not observe loss of tissue during the process, even on isolated cells (fig. S2).

We also stained serial FFPE colorectal cancer tissue sections and shuffled the order of the primary Abs used for iterative staining cycles on each slide. We then quantified the various markers on these serial sections and observed no significant differences in the density of positive cells found in untreated slides and slides that underwent several staining, destaining, and restaining cycles (Fig. 3,

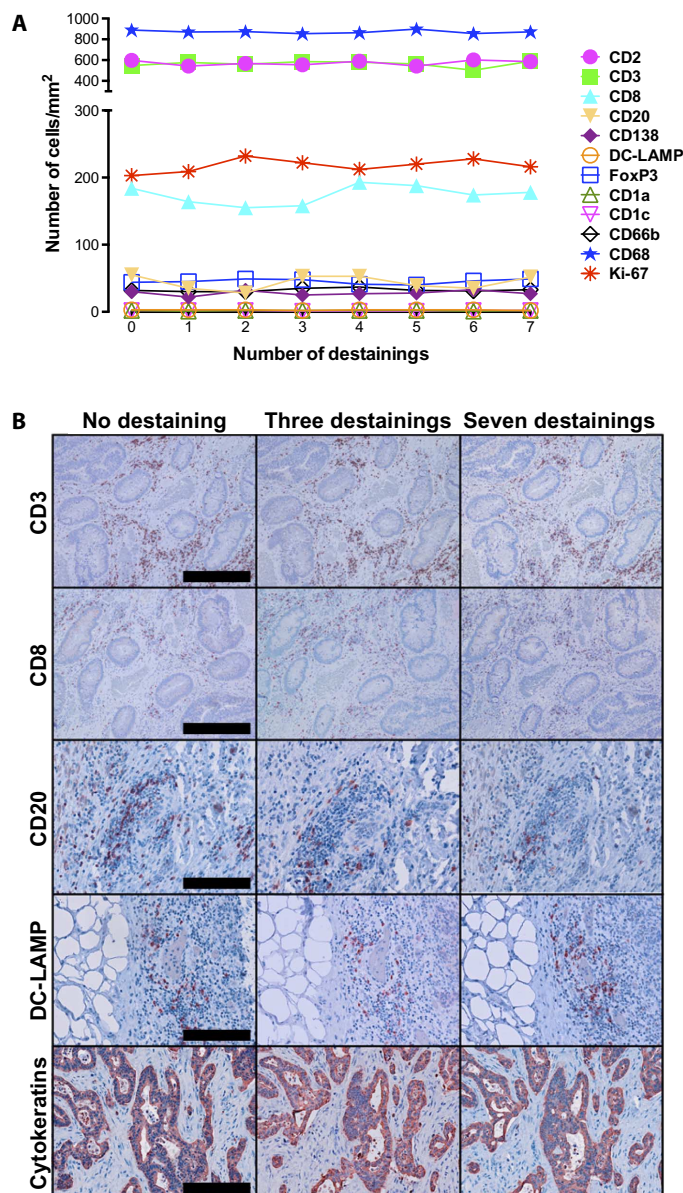


Fig. 3. MICSSS does not alter tissue antigenicity. (A) A series of 12 adjacent 5-μm FFPE sections were obtained from a colorectal tumor tissue, and each slide was stained with a panel of Abs using the MICSSS workflow but in a different Ab sequence order for each slide. Line graph shows the densities of tumor-associated immune cells positive for CD1a, CD1c, CD2, CD3, CD8, CD20, CD66b, CD68, CD138, FoxP3, DC-LAMP, and Ki-67 whether each marker was stained before or after one to seven destaining cycles. (B) Representative pictures revealed similar staining intensity whether the marker was stained before or after several staining/destaining cycles. Scale bars, 200 μm.

A and B), suggesting that tissue antigen expression was not affected during the staining and destaining process. Notably, however, markers with low and heterogeneous expression level (for example, PD-L1) could be affected by numerous cycles of staining/destaining and should be prioritized in the staining.

To address whether consecutive destaining can alter signal intensity, we stained again serial sections with a shuffled Ab sequence following the MICSSS workflow. After image acquisition, the pictures were subjected to color deconvolution. Then, the intensity histograms of pixels corresponding to chromogen were analyzed, revealing similar signal intensities after several cycles of destaining/restaining cycles (fig. S3) and establishing that MICSSS does not significantly alter the antigenicity of any of the markers tested. Additionally, we found that destained slides can be successfully restained even after several months of storage, allowing prolonged slide storage for future use as new markers become available.

Another potential caveat of repetitive Ab incubation is the potential associated steric hindrance due to remaining Abs. We stained for different antigens expressed by the same cellular compartments using the MICSSS method. We were able to detect multiple markers expressed on the same cell (fig. S4, A to C), including CD2⁺ CD3⁺ CD8⁺ triple-positive T cells, CD2⁺ CD3⁺ CD8⁻ PD-1⁺ T follicular helper cells (fig. S4A), and HLA-DR⁺ CD206⁺ CD163⁺ CD68⁺ quadruple-positive macrophages (fig. S4B). No steric hindrance was observed because we were able to visualize cytoplasmic, nuclear, and cellular markers on the same cellular compartment (fig. S4C). The absence of steric hindrance was further confirmed upon successful consecutive cycles of staining/bleaching using the same marker (fig. S5).

MICSSS can be generated while preserving a fixed diagnostic marker

Pathology rules and regulations at some institutions may require storing stained slides for prolonged periods of time, thus preventing the destaining of diagnostic markers. To address whether diagnostic markers could be preserved while generating multiple consecutive stainings, we developed a destaining procedure that will allow us to remove the AEC stain without affecting other chromogens. Figure 4 shows lung tumor FFPE tissue section stained with anti-cytokeratin Abs and revealed with the chromogen 3,3'-diaminobenzidine (DAB). Then, the slide was stained consecutively for B cells (CD20), marker of cell proliferation (Ki-67), mature DCs (DC-LAMP), and plasma cells (CD138) and revealed with the AEC chromogen. The cytokeratin/DAB stain remained untouched, whereas the AEC stain was removed after each staining cycle, confirming that the MICSSS method can be used even if long-term storage of stained slides is required.

MICSSS helps profile tumor response to checkpoint blockade

Recent studies of tumor lesions treated with checkpoint blockade have highlighted the need to assess immune cell distribution and phenotype in the TME based on their predictive value for clinical benefit (15, 16). Here, we asked whether MICSSS could be used to track longitudinal immune cell changes in tumor lesions treated with immunotherapy regimen. Thus, we analyzed five pretreatment/posttreatment tissue pairs obtained from five cutaneous melanoma patients before and after treatment with anti-CTLA-4 monoclonal Ab (ipilimumab) using MICSSS.

Tumor tissue sections were stained for PD-L1, myeloid (CD68 and DC-LAMP), and lymphoid populations (CD20, CD3, and FoxP3) (movie S1). Stained sections were scanned, and pictures were analyzed

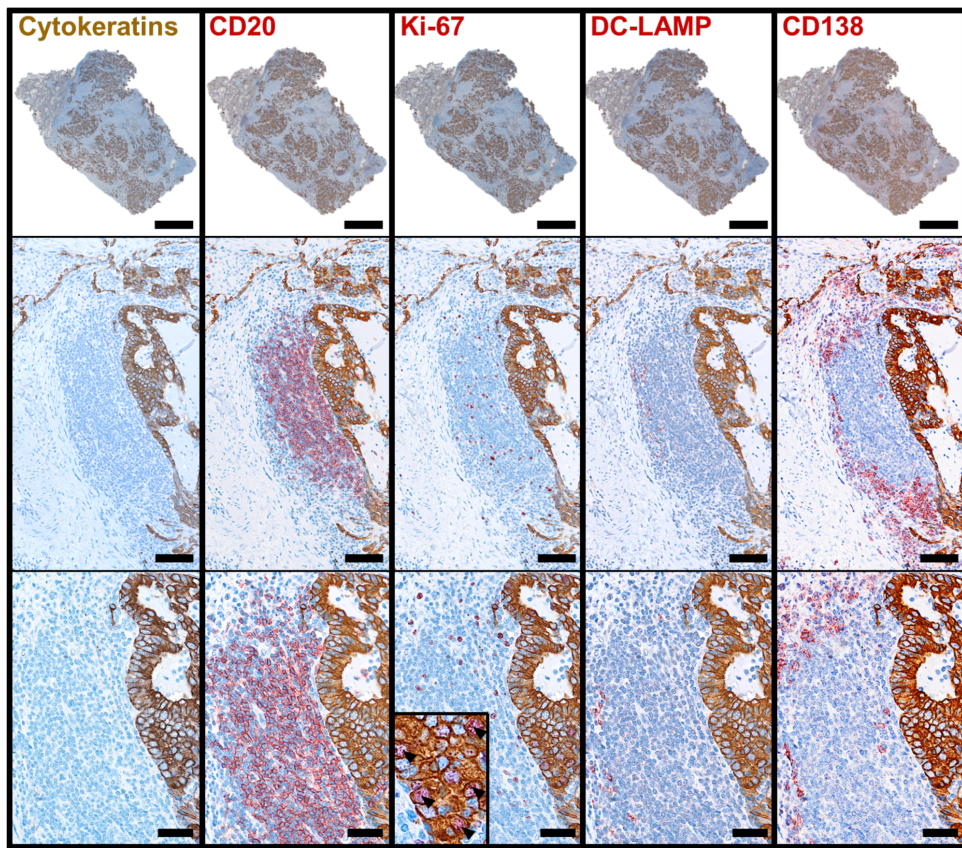


Fig. 4. MICSSS can selectively remove one chromogen-stained marker while preserving a fixed diagnostic marker. Lung adenocarcinoma tissue section was permanently stained with anti-cytokeratin Abs (clones AE1 and AE3) revealed by DAB (brown) and sequentially stained and destained with anti-CD20, anti-Ki-67, anti-DC-LAMP, and anti-CD138 Abs and revealed by AEC in red. The cytokeratin staining was kept as a reference along the staining process because the destaining process, which selectively removed only the AEC stain, did not affect it. Scale bars, 2 mm, 100 μ m, and 50 μ m for the upper, middle, and lower panels, respectively.

using image processing software and quantified using CellProfiler (Table 1). We found that PD-L1 staining was heterogeneous between patients (Fig. 5A) and expressed both on tumor cells and on tumor-associated CD68⁺ macrophages and DC-LAMP⁺ mature DCs (Fig. 5, B and C). Multiparameter image analysis revealed a wide range of PD-L1 expression on macrophages (5 to 90%) and mature DCs (0 to 90%) (Table 1). We also observed ectopic lymphoid structures (also called tertiary lymphoid structures) in 4 of 10 tissue samples. These structures were organized in B cell follicles, adjacent to T cell areas, and contained antigen-presenting cells including CD68⁺ macrophages and DC-LAMP⁺ mature DCs (Fig. 5A). If no conclusion about predictive value can be drawn because of the small number of patients analyzed, our data show that MICSSS can be used to track changes in complex immune subsets *in situ* throughout therapy (movie S1).

MICSSS can identify immune prognostic markers in cancer patients

To determine whether MICSSS can be used for the identification of immune prognostic markers in lung cancer (12), tissue cores obtained from the center of tumors isolated from 75 non–small cell lung cancer (NSCLC) patients were analyzed on a single slide in a tissue microarray (TMA) format. The tissue cores were stained with a 10-plex marker panel that included CD3 (marker of all lymphocytes), CD20 (marker of B cells), FoxP3 (marker of regulatory/activated T cells),

CD68 (marker of macrophages), CD66b (marker of neutrophils), DC-LAMP (marker of mature DCs), CD1c (marker of DC and B cell subsets), major histocompatibility complex (MHC) class I, Ki-67 (marker of cell proliferation), and cytokeratin (marker of normal and neoplastic tissue of epithelial origin).

The MICSSS analyses helped reveal interindividual heterogeneity in the density of tumor-infiltrating immune cells, as previously reported (4). Representative examples of tumors with high or low CD3-, CD20-, FoxP3-, CD68-, CD66b-, DC-LAMP-, CD1c-, and Ki-67-positive cell densities as well as high and low MHC class I expression are shown in Fig. 6A. We also found statistically significant correlations between patients' overall survival and density of tumor-associated CD3⁺ ($n = 75$; $P = 0.0046$, log-rank test), FoxP3⁺ ($n = 75$; $P = 0.01$, log-rank test), CD68⁺ ($n = 75$; $P = 0.036$, log-rank test), CD66b⁺ ($n = 75$; $P = 0.046$, log-rank test), DC-LAMP⁺ ($n = 75$; $P < 0.0001$, log-rank test), and CD1c⁺ ($n = 75$; $P = 0.008$, log-rank test) cells (Fig. 6B). Coexpression analyses showed that CD1c was found on both B cells and DCs but that the prognostic value of CD1c⁺ cells was mostly attributable to DCs (CD1c⁺ CD20⁻ cells) (fig. S6). Loss of MHC class I expression was a significant indicator of poor prognosis ($n = 75$; $P = 0.049$, log-rank test). There was no significant correlation between the density of CD20⁺ B cells and improved overall survival ($n = 75$; $P = 0.42$, log-rank test; Fig. 6B). Tumor and immune cell proliferation (Ki-67-T and Ki-67-I, respectively, based on marker colocalization) were not significantly

Table 1. Comparative IHC analysis of melanoma lesions before and after treatment with ipilimumab.

	Responders (<i>n</i> = 3)		Nonresponders (<i>n</i> = 2)	
	Before ipilimumab	After ipilimumab	Before ipilimumab	After ipilimumab
CD3 ⁺ (cells/mm ²), mean (min–max)	3542 (44–6375)	2998 (357–5005)	1657 (100–3214)	1785 (26–3544)
CD3 ⁺ FoxP3 ⁺ (cells/mm ²), mean (min–max)	150 (3–442)	256 (162–420)	125 (50–200)	320 (3–637)
CD20 ⁺ (cells/mm ²), mean (min–max)	472 (1–1411)	574 (112–1031)	73 (32–113)	754 (2–1514)
CD68 ⁺ (cells/mm ²), mean (min–max)	574 (212–1040)	773 (716–850)	1138 (1085–1190)	495 (98–891)
DC-LAMP ⁺ (cells/mm ²), mean (min–max)	40 (1–115)	20 (7–28)	18 (14–21)	11 (1–20)
CD68 ⁺ PD-L1 ⁺ (%), mean (min–max)	43 (5–90)	53 (30–90)	55.5 (38–73)	23.5 (8–39)
DC-LAMP ⁺ PD-L1 ⁺ (%), mean (min–max)	20 (0–35)	76 (66–90)	45.5 (44–47)	34.5 (0–69)

associated with overall survival (*n* = 75; *P* = 0.23 and *P* = 0.11, respectively, log-rank test). Combined analysis of the presence of DC-LAMP⁺ mature DCs and CD66b⁺ neutrophils (Fig. 6C) in tumors revealed that tumor lesions that were poor in DCs and rich in neutrophils (DC-LAMP^{low} and CD66b^{high}; *n* = 6) correlated with reduced overall survival, whereas DC-LAMP^{high}/CD66b^{low} tumors (*n* = 35) correlated with increased overall survival (70% overall survival at 8 years; *n* = 75; *P* < 0.0001, log-rank test). The density of tumor-associated mature DCs helped subcategorize early-stage patients (TNM stages I and II) and late-stage patients (TNM stages III and IV) into good and poor prognosis groups (Fig. 6C). Analysis of mature DC density helped identify patients with high tumor-associated CD3⁺ T cell densities but with poor prognosis (Fig. 6C). Using Cox multivariate regression analyses on this small cohort of patients, patient age, TNM stage, and CD66b/DC-LAMP score were significantly and independently associated with overall survival [hazards ratio (HR), 2.473, 3.113, and 0.476; *P* = 6.78 × 10⁻³, 2.09 × 10⁻⁴, and 4.97 × 10⁻⁵, respectively, Cox regression; *n* = 75; Table 2]. Although these results need to be validated on larger cohort of patients, these data show that MICSSS can help screen and validate comprehensive panels of prognostic factors or help discover new prognostic markers in a sample-sparing manner.

Digital cartography of tumors allows multiparameter analysis at the cellular level

The key potential of our complex multiplexed assays is to provide a detailed analysis of the composition and spatial distribution of the different cell populations in tissue specimens, allowing a digital cartography of the tumor tissue and complex multiparametric description of key cell populations. To perform these analyses in the setting of large clinical trials, it is critical to generate a high-throughput and robust image analysis approach. To address this need, we developed an automated spatial alignment of digital whole-slide images of the different stains. For highest robustness, we implemented positive cell recognition using convolutional neural networks, a type of “deep learning” algorithm, and connected component and statistical analysis to extract

cell counts for single and multipositive cells. This analysis provides multiple images containing all pixels positive for each biomarker. These images are then integrated into the desired digital landscape map of the tissue lesion containing a multiparametric description of biomarker-stained positive cells. Complete description of this pipeline is provided in the Supplementary Materials. As a proof of concept, we applied this methodology to identify single-positive CD3 and Ki-67 cells as well as double-positive (CD3⁺ Ki-67⁺) proliferating T cells in the lung cancer TMA. Movie S2 shows cells marked computationally in green that are double-positive for CD3 and Ki-67 in two different tumors identifying low and high T cell proliferation state. As shown in fig. S7, significant correlations (*r* = 0.907, *P* = 3.4 × 10⁻²⁹ and *r* = 0.901, *P* = 3.7 × 10⁻²⁸, Spearman test; *n* = 75) were found between manual quantification (done by two independent observers) and fully automatic quantifications using our new automated image software, validating the accuracy of our fully integrated approach.

DISCUSSION

Here, we describe a simple, highly sensitive, multiplexed chromogen-based IHC method, which we called MICSSS, to comprehensively characterize tissue cell phenotype, state, and spatial distribution in inflammatory lesions. Although MICSSS was initially developed to map the TME, our method can be easily used to analyze other tissue types.

The MICSSS method does not lead to antigenicity loss, steric hindrance, or increased cross-reactivity. MICSSS implementation does not require additional instrumentation and relies on standard antigen retrieval and staining protocols, limiting the need for validation strategies, making MICSSS a method of choice for multiplexed IHC in routine clinical pathology laboratories.

Several cutting edge methods for high-dimensional tissue analysis have been developed (19, 22). Tissue mass cytometry, which could optimally stain for large Ab panels, requires tissue vaporization, has low resolution (1 μm) and low sample throughput because of slow

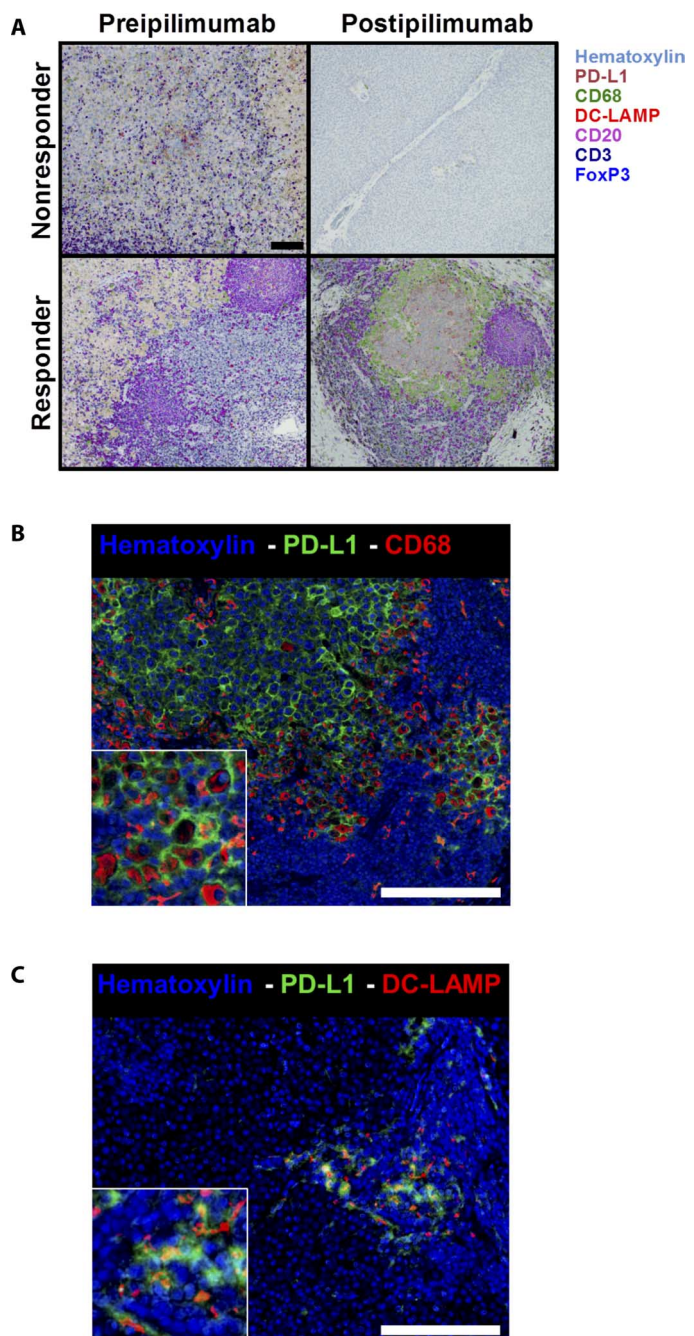


Fig. 5. MICSSS helps monitor tumor response to immunotherapy regimen. (A) FFPE melanoma tissue sections ($5\ \mu\text{m}$) isolated before and after treatment with ipilimumab from one responder and one nonresponder patient were stained following the MICSSS method. Each tissue section was stained sequentially with hematoxylin and anti-PD-L1, anti-CD68, anti-DC-LAMP, anti-CD20, anti-CD3, and anti-FoxP3 Abs, and images were overlaid. (B and C) Images show the expression of PD-L1 by either CD68 $^{+}$ macrophages (B) or DC-LAMP $^{+}$ mature DCs (C) in a responder patient. Scale bars, $100\ \mu\text{m}$.

image acquisition, and will remain (for some time at least) restricted to selected academic centers. Other multiplex platforms such as Vectra (PerkinElmer) or MultiOmyx (GE Healthcare) have inherent limitations that include the use of costly materials and fluorescent dyes that are light-sensitive and induce spectral overlap, low sample throughput due

to slow whole-slide image scanning, and image analyses limited to defined fields.

In the meantime, the need for monitoring of tissue inflammatory lesions in response to the flurry of immunomodulation strategies for the treatment of cancer and inflammatory disease has never been more pressing (17, 23). In cancer, in particular, immunotherapy strategies have led to significant clinical responses, yet these responses remain limited to a subset of patients, and the mechanisms that lead to response or no response to immunotherapy agents remain elusive (24, 25). Recent results have revealed that in patients responding to checkpoint blockade, T cells infiltrate the center of the tumors, whereas T cells remain at the edge, often associated with macrophages and dense network of fibroblasts, in patients who do not respond to checkpoint blockade (15, 16). These results highlight the need for the inclusion of longitudinal high-dimensional analysis of tissue lesions in immune monitoring strategies, and MICSSS is best poised to serve this need. As an example, we show that MICSSS can be used as a new tool to describe the immune microenvironment at baseline and track immune changes upon therapy, providing a unique sample-sparing analytical tool to characterize limited tissue samples obtained during clinical studies.

By analyzing the composition of complex immune cell populations that accumulated in the center of 75 primary NSCLC tumor lesions, we found that a neutrophil/DC density score refined the prognostic value of tumors rich in T cells and was the best independent prognosticator ($n = 75$; $P = 4.97 \times 10^{-5}$, Cox regression), even stronger than the TNM stage ($n = 75$; $P = 2.09 \times 10^{-4}$, Cox regression). Although these findings will obviously need to be validated on a larger number of patients, these data reveal the potential of MICSSS to expand the Immunoscore prognostic signature of human tumor lesions in a clinically relevant manner.

In addition to developing a new multiplexed IHC method, we also designed an automated digital landscaping method to evaluate the density and spatial distribution of complex cell populations in a high-throughput manner based on neural network marker identification and quantification on whole slides. The combination of both technologies reveals the power of multiplexed biomarker imaging and quantitative analysis for in-depth tissue analysis.

Here, we showed that the use of the MICSSS method might improve the characterization of immune changes at the tumor site upon treatment, the finding of predictive correlates of response to treatment, and the identification of prognostic markers. However, the small number of samples limits data interpretation, and validation on larger cohort of patients is needed. The MICSSS throughput is currently a main limitation of the MICSSS method, but automation of the process should overcome this disadvantage. Even if we have not yet identified antigens whose expression was impaired by the repetitive destaining/restaining method, we do not exclude that antigenicity loss can occur for some antigens, and recommend staining for potential weaker markers such as PD-L1 first.

In summary, we described a multiplexed chromogenic IHC strategy for high-dimensional tissue analysis that circumvents many of the limitations of regular chromogenic, immunofluorescence, and mass cytometry approaches that could be readily implemented in clinical pathology laboratories. The MICSSS method provides a new powerful tool to map the microenvironment of tissue lesional sites with excellent resolution, in a sample-sparing manner, to monitor immune changes *in situ* during therapy and help identify prognostic and predictive markers of clinical outcome in patients with cancer and inflammatory diseases.

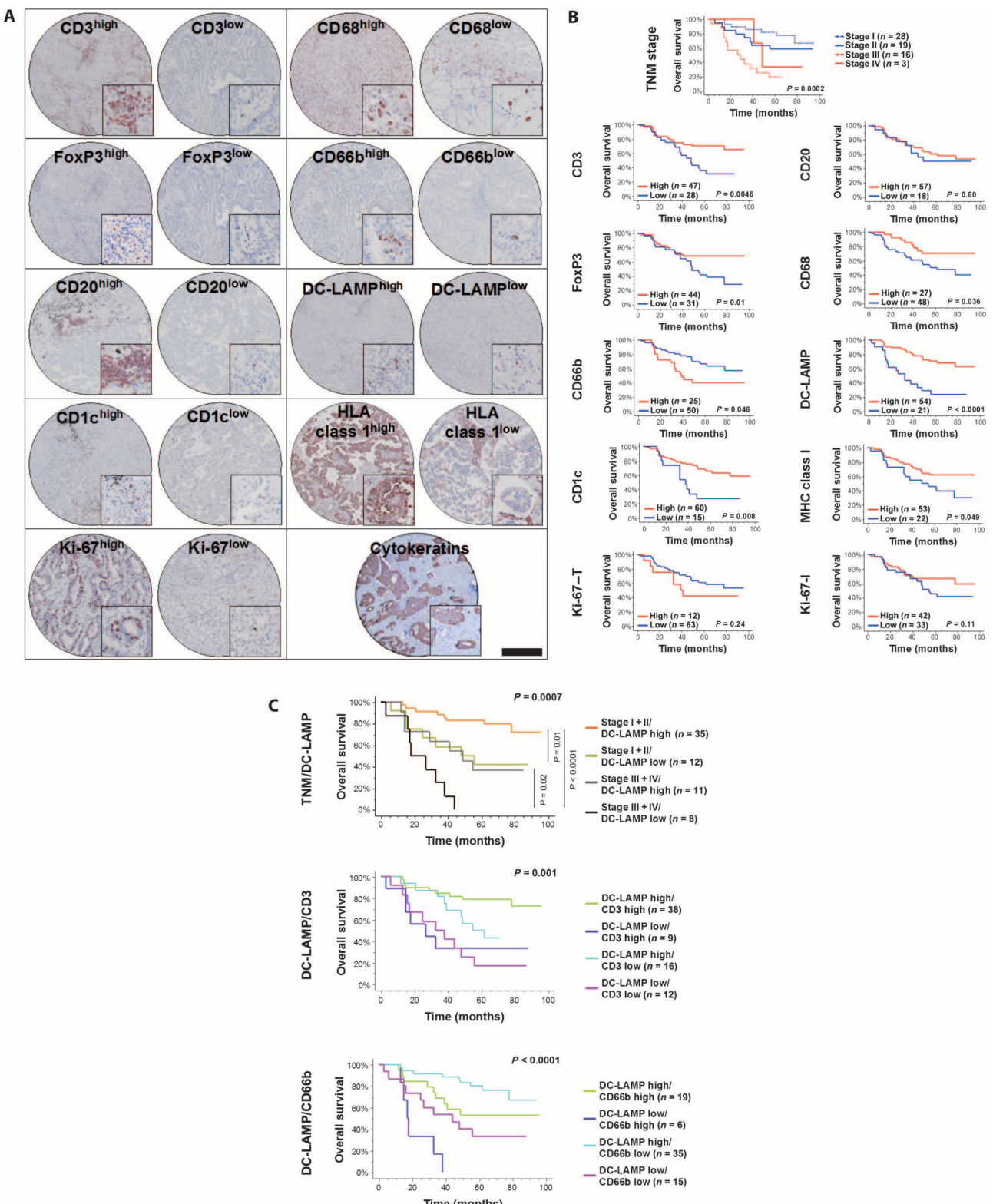


Fig. 6. MICSS helps identify immune prognostic markers in cancer patients. (A) Representative images of different biopsy sections obtained from NSCLC TMA sequentially stained with anti-CD3, anti-CD20, anti-FoxP3, anti-CD68, anti-CD66b, anti-DC-LAMP, anti-CD1c, anti-MHC class I, anti-Ki-67, and anti-cytokeratin Abs. Scale bar, 0.5 mm. (B) Kaplan-Meier curves illustrate the duration of overall survival according to the TNM stage and the densities of CD3⁺, CD20⁺, FoxP3⁺, CD68⁺, CD66b⁺, DC-LAMP⁺, CD1c⁺, Ki-67⁺, and MHC class I⁺ cells. Red lines represent high cell densities (or high expression) and blue lines represent low densities (or low expression). (C) Kaplan-Meier curves illustrate the duration of overall survival according to the combined analysis of TNM stage and immune cell densities (CD3⁺, DC-LAMP⁺, and CD66b⁺).

Table 2. Multivariate Cox proportional hazards analyses for overall survival according to clinical parameters and immune cell densities in NSCLC. CI, confidence interval.

	HR (95% CI)	P
TNM stage (I/II/III/IV)	2.407 (1.513–3.828)	2.09×10^{-4}
Age (<60 years versus >60 years)	3.113 (1.368–7.082)	6.78×10^{-3}
CD66b/DC-LAMP score (LoHi/HiHi/LoLo/HiLo)	0.474 (0.330–0.680)	4.97×10^{-5}

MATERIALS AND METHODS

Patients

Paraffin-embedded human tonsils, ulcerative colitis, NSCLC, melanoma, and colorectal tumor samples were obtained from the Biorepository tissue bank at the Icahn School of Medicine at Mount Sinai (ISMMS). Tissue samples were obtained according to protocols approved by the Institutional Review Board (IRB) of ISMMS. J.D.W. and T.M. provided melanoma tumor lesions treated with ipilimumab. Patients with metastatic melanoma who were treated with ipilimumab were selected for inclusion in this analysis on the basis of sample availability and annotated clinical data. Clinical benefit was determined by evidence of tumor burden reduction or prolonged stable disease lasting at least 9 months after initiation of ipilimumab. Patients received ipilimumab at 3 or 10 mg/kg as per initial study design. Two different tissue lesions were obtained from tumor excision before and after treatment with ipilimumab and analyzed by IHC. All patients provided informed consent to an IRB-approved correlative research protocol before the collection of tissue (Memorial Sloan Kettering Cancer Center IRB #00–144). TMA displaying 75 lung adenocarcinomas was purchased from U.S. Biomax Inc. The TMA contained human tissues obtained with informed consent according to U.S. federal law. The Reporting Recommendations for Tumor Marker Prognostic Studies (REMARK) criteria (26) were followed throughout this study.

Immunohistochemistry

FFPE tissue sections (5 μ m) were deparaffinized in xylene and rehydrated in decreasing concentrations of ethanol (100, 90, 70, and 50% and distilled water; 5 min each). Rehydrated tissue sections were incubated in pH 6 or pH 9 Target Retrieval Solution (Dako, S2369 and S2367) for antigen retrieval at 95°C for 20 to 30 min. Tissue sections were incubated in 3% hydrogen peroxide for 15 min to block endogenous peroxidase activity and in serum-free protein block solution (Dako, X0909) for 30 min to block free Fc receptor binding sites before adding the primary Abs, listed in table S1, followed by biotinylated secondary Abs. Binding of biotinylated Abs was revealed using streptavidin-HRP, and chromogenic revelation was performed using AEC (Vector, SK-4200) or DAB (Dako, K3468). Polymer-HRP detection system (Dako) might also be used. Nonspecific isotype controls were used as negative controls. Tissue sections were then counterstained with Harris' modified hematoxylin (Sigma, HHS16), mounted with aqueous mounting medium (Dako, C0563), and scanned for digital imaging and quantification (Olympus whole-slide scanner with OlyVIA software or Nikon Eclipse Ci-E microscope). After scanning, slide coverslips were removed in hot (~50°C) water, and tissue sections were destained in organic solvent (50% ethanol, 2 min; 100% ethanol, 2 min; 100% xylene; 2 min, 100% ethanol, 2 min; and 50% ethanol,

2 min). This step removed staining with labile AEC precipitate while leaving DAB unaffected. Then, the slides were washed in distilled water for 5 min, mounted with aqueous mounting medium (Dako, C0563), and stored at 4°C up to several months or directly subjected to the next round of staining as previously described with some modifications. Antigen retrieval was performed before incubating each slide with 3% hydrogen peroxide plus 1 mM sodium azide for 20 min and in serum-free protein block solution (Dako) for 30 min. Slides were then blocked with 5% serum and monovalent Fab fragment for 30 min. Serum (Jackson ImmunoResearch) was from the same species than the previous primary Ab used, and Fab fragment (Jackson ImmunoResearch) was directed against the same species than the primary Ab used previously. Biotins were blocked using the biotin-blocking system (X0590, Dako). No biotin-blocking system was done after polymer-HRP detection system usage. Then, the tissue sections were stained as previously described.

Melanin bleaching

All melanoma tissue sections were incubated in 3% hydrogen peroxide plus 1% Na₂HPO₄ solution for 12 hours at room temperature before incubation with primary Abs to remove the melanin granules.

Microscopy and image analysis

Images were acquired using an Olympus whole-slide scanner with OlyVIA software or a Nikon Eclipse Ci-E microscope. Each stain was artificially attributed a color code, and images were overlaid using ImageJ or Adobe Photoshop CS6. Pixel colocalization was assessed by calculating Manders' overlap coefficient with threshold set by Costes method (tM) using Fiji (Coloc 2 plug-in). Tissue-associated immune cell densities were measured in a blinded fashion without the knowledge of clinical characteristics or outcome as previously described (11) on the whole tissue (for the TMAs) or on the three most infiltrated fields (27) and validated using CellProfiler 2.1.1 (Broad Institute) (28). Significant correlation was found between manual and automatic quantifications ($r = 0.99$ and $P < 0.0001$, Spearman test). Immune cell density was expressed as an absolute number of positive cells per square millimeter. The density of MHC class I⁺ cells was also assessed semiquantitatively as 1 (<25% of positive cells), 2 (25 to 50%), 3 (51 to 75%), or 4 (>75%). The density of Ki-67-positive immune (KI-67-I) or tumor (Ki-67-T) cells was assessed semiquantitatively as low ($\leq 10\%$) or high ($>10\%$) density.

Automated image analysis

Spatial alignment of whole-slide images

The whole-slide image of the Ki-67-stained TMA was spatially aligned to the CD3-stained whole-slide image. The images were first roughly aligned using a template matching technique at low resolution (64 times downsampled). This resulted in an initial translation vector and a rotation angle to map the positions in the CD3-stained slide to the Ki-67-stained slide. Subsequently, the elastix toolbox was used to obtain the affine transformation to minimize the differences between the images (using normalized mutual information as a metric) (29, 30). The resultant combined transformation can be used to obtain, for each position in the CD3-stained slide, the corresponding position in the Ki-67-stained slide. This approach does not address small, local deformations, but these are expected to be minimal because of the careful multiplexing procedure.

Positive cell detection using convolutional neural networks

In each stained slide, positive cells were identified through the use of convolutional neural networks, used mainly in generic computer vision

tasks (31). Our approach is similar to the one presented by Cireşan *et al.* (32) for the detection of mitosis in hematoxylin and eosin-stained images of breast cancer. First, an observer (G.L.) annotated 3500 positive nuclei across all TMA spots and indicated regions containing normal tissue and tar to serve as the negative class. Subsequently, 45 by 45 pixel patches were sampled from the positive nuclei and the background regions to train a five-layer convolutional network. This network was then used to estimate the posterior likelihood of being part of a positive nucleus for each pixel in the CD3 and Ki-67 whole-slide images. To prevent any bias in the results, this training/classification step was performed in a twofold cross-validation, where half of the TMA spots served as training data and half were classified.

Postprocessing steps and cell counting

To extract the center pixels for each nucleus, we applied a fast radial symmetry transform approach to the generated likelihood maps (33). This step helped remove false positive in dense cell clusters by focusing only on radially symmetric objects (for example, cell nuclei) and identified their center pixels.

The registration transformation, for each positive pixel in the CD3-stained image, helped assess additional positive pixel in the Ki-67-stained image. These data resulted in three images: one containing all the pixels that were CD3-positive, one containing all the pixels that were Ki-67-positive, and one containing all the double-positive pixels. Connected component analysis was subsequently applied to extract the total number of positive cells for each of these images. Thus, for each TMA spot, the total number of CD3-, Ki-67-, and double-positive cells was obtained.

Statistical analysis

Sample size calculation for the prognostic biomarker analysis was performed using the method described by Schoenfeld (34). For each biomarker, the proportions of patients in low and high groups were based on published studies reviewed by Remark *et al.* (12). Associations of variables to prognosis were visualized using the Kaplan-Meier method, and significant differences of overall survival among patient groups were calculated with the log-rank test. The following cutoffs were used to discriminate low and high groups for the survival analyses using the “minimum *P* value approach” (6): 130.3 cells/mm² (CD68), 9.8 cells/mm² (CD66b), 0.42 cells/mm² (DC-LAMP), 1.13 cells/mm² (CD1c), 1.27 cells/mm² (CD20), 59.1 cells/mm² (CD3), 7.5 cells/mm² (FoxP3), 25% (Ki-67-T), and 10% (Ki-67-I). To avoid overfitting, we corrected overall survival log-rank *P* values obtained using the minimum *P* value approach, as previously reported (6). We used multivariate Cox proportional hazards model to determine HRs. To conduct regression with categorical variables, each variable was coded before it was entered into the Cox model. Proportional hazards assumption was assessed and respected for each variable. Correlations were evaluated by the nonparametric Spearman test. All *P* values were calculated using two-sided tests. *P* values <0.05 were considered statistically significant. Analyses were performed using GraphPad Prism version 6.00 and R version 3.1.3 (www.r-project.org/).

SUPPLEMENTARY MATERIALS

immunology.science.org/cgi/content/full/1/1/aaf6925/DC1

Fig. S1. Efficiency assessment of the blocking method.

Fig. S2. MICSSS does alter tissue integrity.

Fig. S3. MICSSS does not alter the signal intensity.

Fig. S4. Visualization of multiple antigens on single cells using MICSSS.

Fig. S5. Sequential CD3 staining using MICSSS.

Fig. S6. Prognostic value of CD1c-positive cells.

Fig. S7. Correlation between automatic and manual quantifications.

Table S1. Primary Abs used for IHC.

Movie S1. Sequential staining using MICSSS on melanoma after ipilimumab treatment.

Movie S2. Automated image solution for multiparameter analysis at the cellular level.

REFERENCES AND NOTES

- M. E. De Obaldia, A. Bhandoola, Transcriptional regulation of innate and adaptive lymphocyte lineages. *Annu. Rev. Immunol.* **33**, 607–642 (2015).
- H. Spits, T. Cupedo, Innate lymphoid cells: Emerging insights in development, lineage relationships, and function. *Annu. Rev. Immunol.* **30**, 647–675 (2012).
- S. A. van de Pavert, R. E. Mebius, New insights into the development of lymphoid tissues. *Nat. Rev. Immunol.* **10**, 664–674 (2010).
- W. H. Fridman, F. Pagès, C. Sautès-Fridman, J. Galon, The immune contexture in human tumours: Impact on clinical outcome. *Nat. Rev. Cancer* **12**, 298–306 (2012).
- S. Shalapour, M. Karin, Immunity, inflammation, and cancer: An eternal fight between good and evil. *J. Clin. Invest.* **125**, 3347–3355 (2015).
- J. Galon, A. Costes, F. Sanchez-Cabo, A. Kirillovsky, B. Mlecnik, C. Lagorce-Pagès, M. Tosolini, M. Camus, A. Berger, P. Wind, F. Zinzindohoué, P. Brunéval, P.-H. Cugnenc, Z. Trajanoski, W.-H. Fridman, F. Pagès, Type, density, and location of immune cells within human colorectal tumors predict clinical outcome. *Science* **313**, 1960–1964 (2006).
- W. H. Fridman, R. Remark, J. Goc, N. A. Giraldo, E. Becht, S. A. Hammond, D. Damotte, M.-C. Dieu-Nosjean, C. Sautès-Fridman, The immune microenvironment: A major player in human cancers. *Int. Arch. Allergy Immunol.* **164**, 13–26 (2014).
- J. Galon, H. K. Angell, D. Bedognetti, F. M. Marincola, The continuum of cancer immuno-surveillance: Prognostic, predictive, and mechanistic signatures. *Immunity* **39**, 11–26 (2013).
- J. Galon, F. Pagès, F. M. Marincola, H. K. Angell, M. Thurin, A. Lugli, I. Zlobec, A. Berger, C. Bifulco, G. Botti, F. Tatangelo, C. M. Britten, S. Kreiter, L. Chouchane, P. Delrio, H. Arndt, M. Asslaber, M. Maio, G. V. Masucci, M. Mihm, F. Vidal-Vanaclocha, J. P. Allison, S. Gnijatic, L. Hakansson, C. Huber, H. Singh-Jasuja, C. Ottensmeier, H. Zwierzina, L. Laghi, F. Grizzi, P. S. Ohashi, P. A. Shaw, B. A. Clarke, B. G. Wouters, Y. Kawakami, S. Hazama, K. Okuno, E. Wang, J. O'Donnell-Tormey, C. Lagorce, G. Pawelec, M. I. Nishimura, R. Hawkins, R. Lapointe, A. Lundqvist, S. N. Khleif, S. Ogino, P. Gibbs, P. Waring, N. Sato, T. Torigoe, K. Itoh, P. S. Patel, S. N. Shukla, R. Palmqvist, I. D. Nagtegaal, Y. Wang, C. D'Arrigo, S. Kopetz, F. A. Sinicrope, G. Trinchieri, T. F. Gajewski, P. A. Ascierto, B. A. Fox, Cancer classification using the Immunoscore: A worldwide task force. *J. Transl. Med.* **10**, 205 (2012).
- J. Goc, C. Germain, T. K. D. Vo-Bourgais, A. Lupo, C. Klein, S. Knockaert, L. de Chaisemartin, H. Ouakrim, E. Becht, M. Alifano, P. Validire, R. Remark, S. A. Hammond, I. Cremer, D. Damotte, W.-H. Fridman, C. Sautès-Fridman, M.-C. Dieu-Nosjean, Dendritic cells in tumor-associated tertiary lymphoid structures signal a Th1 cytotoxic immune contexture and license the good positive prognostic value of infiltrating CD8⁺ T cells. *Cancer Res.* **74**, 705–715 (2014).
- R. Remark, M. Alifano, I. Cremer, A. Lupo, M.-C. Dieu-Nosjean, M. Riquet, L. Crozet, H. Ouakrim, J. Goc, A. Cazes, J.-F. Fléjou, L. Gibault, V. Verkarre, J.-F. Régnard, O.-N. Pagès, S. Ouard, B. Mlecnik, C. Sautès-Fridman, W.-H. Fridman, D. Damotte, Characteristics and clinical impacts of the immune environments in colorectal and renal cell carcinoma lung metastases: Influence of tumor origin. *Clin. Cancer Res.* **19**, 4079–4091 (2013).
- R. Remark, C. Becker, J. E. Gomez, D. Damotte, M.-C. Dieu-Nosjean, C. Sautès-Fridman, W.-H. Fridman, C. A. Powell, N. K. Altoriki, M. Merad, S. Gnijatic, The non-small cell lung cancer immune contexture. A major determinant of tumor characteristics and patient outcome. *Am. J. Respir. Crit. Care Med.* **191**, 377–390 (2015).
- D. M. Pardoll, The blockade of immune checkpoints in cancer immunotherapy. *Nat. Rev. Cancer* **12**, 252–264 (2012).
- D. B. Page, M. A. Postow, M. K. Callahan, J. P. Allison, J. D. Wolchok, Immune modulation in cancer with antibodies. *Annu. Rev. Med.* **65**, 185–202 (2014).
- R. S. Herbst, J.-C. Soria, M. Kowanetz, G. D. Fine, O. Hamid, M. S. Gordon, J. A. Sosman, D. F. McDermott, J. D. Powderly, S. N. Gettinger, H. E. K. Kohrt, L. Horn, D. P. Lawrence, S. Rost, M. Leabman, Y. Xiao, A. Mokatrin, H. Koeppen, P. S. Hegde, I. Mellman, D. S. Chen, F. S. Hodi, Predictive correlates of response to the anti-PD-L1 antibody MPDL3280A in cancer patients. *Nature* **515**, 563–567 (2014).
- P. C. Tumeh, C. L. Harview, J. H. Yearley, I. P. Shintaku, E. J. M. Taylor, L. Robert, B. Chmielowski, M. Spasic, G. Henry, V. Ciobanu, A. N. West, M. Carmona, C. Kivork, E. Seja, G. Cherry, A. J. Gutierrez, T. R. Grogan, C. Mateus, G. Tomasic, J. A. Glaspy, R. O. Emerson, H. Robins, R. H. Pierce, D. A. Elashoff, C. Robert, A. Ribas, PD-1 blockade induces responses by inhibiting adaptive immune resistance. *Nature* **515**, 568–571 (2014).
- J. D. Wolchok, T. A. Chan, Cancer: Antitumour immunity gets a boost. *Nature* **515**, 496–498 (2014).
- D. Robertson, K. Savage, J. S. Reis-Filho, C. M. Isacke, Multiple immunofluorescence labelling of formalin-fixed paraffin-embedded (FFPE) tissue. *BMC Cell Biol.* **9**, 13 (2008).

19. C. Giesen, H. A. O. Wang, D. Schapiro, N. Zivanovic, A. Jacobs, B. Hattendorf, P. J. Schüffler, D. Grolimund, J. M. Buhmann, S. Brandt, Z. Varga, P. J. Wild, D. Günther, B. Bodenmiller, Highly multiplexed imaging of tumor tissues with subcellular resolution by mass cytometry. *Nat. Methods* **11**, 417–422 (2014).
20. M. J. Gerdes, C. J. Sevinsky, A. Sood, S. Adak, M. O. Bello, A. Bordwell, A. Can, A. Corwin, S. Dinn, R. J. Filkins, D. Hollman, V. Kamath, S. Kaanumalle, K. Kenny, M. Larsen, M. Lazare, Q. Li, C. Lowes, C. C. McCulloch, E. McDonough, M. C. Montalto, Z. Pang, J. Rittscher, A. Santamaria-Pang, B. D. Sarachan, M. L. Seel, A. Seppo, K. Shaikh, Y. Sui, J. Zhang, F. Ginty, Highly multiplexed single-cell analysis of formalin-fixed, paraffin-embedded cancer tissue. *Proc. Natl. Acad. Sci. U.S.A.* **110**, 11982–11987 (2013).
21. E. C. Stack, C. Wang, K. A. Roman, C. C. Hoyt, Multiplexed immunohistochemistry, imaging, and quantitation: A review, with an assessment of Tyramide signal amplification, multispectral imaging and multiplex analysis. *Methods* **70**, 46–58 (2014).
22. M. Angelo, S. C. Bendall, R. Finck, M. B. Hale, C. Hitzman, A. D. Borowsky, R. M. Levenson, J. B. Lowe, S. D. Liu, S. Zhao, Y. Natkunam, G. P. Nolan, Multiplexed ion beam imaging of human breast tumors. *Nat. Med.* **20**, 436–442 (2014).
23. A. M. Lesokhin, M. K. Callahan, M. A. Postow, J. D. Wolchok, On being less tolerant: Enhanced cancer immuno-surveillance enabled by targeting checkpoints and agonists of T cell activation. *Sci. Transl. Med.* **7**, 280sr1 (2015).
24. M. A. Postow, J. Chesney, A. C. Pavlick, C. Robert, K. Grossmann, D. McDermott, G. P. Linette, N. Meyer, J. K. Giguere, S. S. Agarwala, M. Shaheen, M. S. Ernstoff, D. Minor, A. K. Salama, M. Taylor, P. A. Ott, L. M. Rollin, C. Horak, P. Gagnier, J. D. Wolchok, F. S. Hodis, Nivolumab and ipilimumab versus ipilimumab in untreated melanoma. *N. Engl. J. Med.* **372**, 2006–2017 (2015).
25. P. Sharma, J. P. Allison, The future of immune checkpoint therapy. *Science* **348**, 56–61 (2015).
26. L. M. McShane, D. G. Altman, W. Sauerbrei, S. E. Taube, M. Gion, G. M. Clark; Statistics Subcommittee of the NCI-EORTC Working Group on Cancer Diagnostics, Reporting recommendations for tumor marker prognostic studies. *J. Clin. Oncol.* **23**, 9067–9072 (2005).
27. M.-G. Anitei, G. Zeitoun, B. Mlecnik, F. Mariot, N. Haicheur, A.-M. Todosi, A. Kirilovsky, C. Lagorce, G. Bindea, D. Ferariu, M. Danciu, P. Bruneval, V. Scripcariu, J.-M. Chevallier, F. Zinzindohoué, A. Berger, J. Galon, F. Pagès, Prognostic and predictive values of the immunoscore in patients with rectal cancer. *Clin. Cancer Res.* **20**, 1891–1899 (2014).
28. T. R. Jones, I. H. Kang, D. B. Wheeler, R. A. Lindquist, A. Papallo, D. M. Sabatini, P. Golland, A. E. Carpenter, CellProfiler Analyst: Data exploration and analysis software for complex image-based screens. *BMC Bioinformatics* **9**, 482 (2008).
29. S. Klein, M. Staring, K. Murphy, M. A. Viergever, J. P. W. Pluim, elastix: A toolbox for intensity-based medical image registration. *IEEE Trans. Med. Imaging* **29**, 196–205 (2010).
30. D. Mueller, D. Vossen, B. Hulskens, Real-time deformable registration of multi-modal whole slides for digital pathology. *Comput. Med. Imaging Graph.* **35**, 542–556 (2011).
31. Y. LeCun, Y. Bengio, G. Hinton, Deep learning. *Nature* **521**, 436–444 (2015).
32. D. C. Cireşan, A. Giusti, L. M. Gambardella, J. Schmidhuber, Mitosis detection in breast cancer histology images with deep neural networks. *Med. Image Comput. Comput. Assist. Interv.* **16**, 411–418 (2013).
33. G. Loy, A. Zelinsky, Fast radial symmetry for detecting points of interest. *IEEE Trans. Pattern Anal. Mach. Intell.* **25**, 959–973 (2003).
34. D. A. Schoenfeld, Sample-size formula for the proportional-hazards regression model. *Biometrics* **39**, 499–503 (1983).

Acknowledgments: We thank Y. A. Jerez for technical assistance and the Biorepository and Pathology Core and the Human Immune Monitoring Core at Mount Sinai for tissue preparation, slide scanning, and technical assistance. **Funding:** M.M. was supported by grants R01CA190400 and R01CA173861. S.G. was supported by the Cancer Research Institute's Clinical Strategy Team and Cancer Vaccine Collaborative grants. S.G. and J.D.W. were supported by grant 1P01CA190174, and T.M. and J.D.W. were supported by the Ludwig Institute and Swim Across America. **Author contributions:** M.M. and S.G. supervised the whole project. M.M., S.G., and R.R. designed the project. R.R. performed the experiments and statistical analyses. M.M., S.G., and R.R. wrote the manuscript. T.M. and J.D.W. provided material. N.G. and G.L. developed the image analysis software. D.D. provided professional expertise. M.M., S.G., and R.R. are inventors of a patent regarding "Tissue profiling using multiplexed immunohistochemical consecutive staining" (patent number pending). **Competing interests:** The authors declare that they have no competing interests.

Submitted 18 March 2016

Accepted 31 May 2016

Published 14 July 2016

10.1126/scimmunol.aaf6925

Citation: R. Remark, T. Merghoub, N. Grabe, G. Litjens, D. Damotte, J. D. Wolchok, M. Merad, S. Gnjatic, In-depth tissue profiling using multiplexed immunohistochemical consecutive staining on single slide. *Sci. Immunol.* **1**, aaf6925 (2016).

In-depth tissue profiling using multiplexed immunohistochemical consecutive staining on single slide

Romain Remark, Taha Merghoub, Niels Grabe, Geert Litjens, Diane Damotte, Jedd D. Wolchok, Miriam Merad and Sacha Gnjatic

Sci. Immunol. 1, aaf6925 (2016)
doi: 10.1126/sciimmunol.aaf6925

Editor's Summary Putting immune cells on the map Multiplexed flow cytometry allows for careful characterization of the complexity of immune cells. However, these cells do not act in isolation, and multiplexed analyses do not extend to spatial visualization of cells in tissue microenvironments. Remark et al. have combined immunohistochemistry with virtual landscaping to generate maps of immune cells in tumors stained with up to 10 distinct antibodies. Rather than using filters to resolve chromogens, they use multiple rounds of staining and destaining, followed by virtual color assignment. This simple yet powerful technique can be used to chart maps of cells in any tissue.

You might find this additional info useful...

This article cites 34 articles, 8 of which you can access for free at:
<http://immunology.science.org/content/1/1/aaf6925.full#BIBL>

Updated information and services including high resolution figures, can be found at:
<http://immunology.science.org/content/1/1/aaf6925.full>

Additional material and information about **Science Immunology** can be found at:
<http://www.sciencemag.org/journals/immunology/mission-and-scope>

This information is current as of October 31, 2016.